

Graph Attention Networks with Physical Constraints for Anomaly Detection

Mohammadhossein Homaei^{a,*}, Iman Khazrak^b, Ruben Molano^a, Andres Caro^a, Mar Avila^a

^aDepartamento de Ingeniería de Sistemas Informáticos y Telemáticos, Universidad de Extremadura, Av/ Universidad S/N, 10003, Cáceres, Extremadura, Spain

^bDepartment of Computer Science, Bowling Green State University, Ohio, USA

Abstract

Water distribution systems (WDSs) face increasing cyber-physical risks, which make reliable anomaly detection essential. Many data-driven models ignore network topology and are hard to interpret, while model-based ones depend strongly on parameter accuracy. This work proposes a hydraulic-aware graph attention network using normalized conservation law violations as features. It combines mass and energy balance residuals with graph attention and bidirectional LSTM to learn spatio-temporal patterns. A multi-scale module aggregates detection scores from node to network level. On the BATADAL dataset, it reaches $F1 = 0.979$, showing 3.3pp gain and high robustness under 15% parameter noise.

Keywords: Graph attention networks, anomaly detection, physics-informed learning, cyber-physical systems, explainable AI

1. Introduction

Water distribution systems (WDSs) are key infrastructures for public health and economy. In recent years, they face more cyber-physical attacks like data manipulation or actuator control [1, 2]. If not detected, such anomalies may cause water loss, service stop, or contamination. SCADA systems collect large sensor data (pressure, flow, tank levels) that support data-based protection [3].

Anomaly detection methods are usually of two kinds. Data-driven ones, such as Deep Learning and Autoencoders [4, 5], often ignore hydraulic topology and act as black boxes, limiting trust [6]. Model-based ones, using simulators like EPANET with residuals [7], give physical sense but depend on uncertain parameters and scale poorly. The challenge is to design a model that is both accurate and interpretable.

This work joins both ideas: physics constraints and neural learning. The question is simple:

Can a GNN that uses physics violation and topology improve anomaly detection in

WDSs, with better robustness and explainability?

We propose the Physics-GAT model with three parts: (i) physics-informed (PI) features from conservation laws, (ii) Graph Attention Network (GAT) for spatial relations, and (iii) Multi-Scale Detection merging local and global scores. On BATADAL, it gets $F1=0.979$ vs 0.946 (gain 3.3 points, Wilcoxon $p = 0.0009$) and detects 10.6% faster (TTD: 1.44h vs 1.61h). Ablation shows PI features are most critical.

Section 2 reviews related works, Section 3 explains the framework, Section 4 presents experiments, Section 5 discusses findings, and Section 6 concludes the paper.

2. Related Work

Early works on WDS anomaly detection used statistical techniques such as CUSUM and EWMA, but these methods had difficulties dealing with the non-linear behavior of SCADA data [8]. Later, machine learning improved the ability to recognize patterns [2], while deep models like autoencoders and CVAEs [4, 5] showed higher accuracy. However, they usually ignore the hydraulic structure of the system and are not easy to interpret [9, 6], learning mostly time dependencies without capturing spatial relations among sensors.

*Corresponding author

Email addresses: mhomaei@alumnos.unex.es (Mohammadhossein Homaei), ikhazra@bgsu.edu (Iman Khazrak), rmolano@unex.es (Ruben Molano), andresc@unex.es (Andres Caro), mmavila@unex.es (Mar Avila)

The BATADAL benchmark [1, 10] introduced C-Town as a reference testbed. Its best solution used EPANET simulation combined with residual analysis [7], showing the value of physics-based detection. Still, such methods depend on parameters like pipe roughness and water demand, which are often unknown in old networks, reducing their stability and generalization.

More recent graph-based approaches (GCN, GraphSAGE [9]) include the network topology but do not directly use the physical conservation laws. PI-neural networks have achieved good results in other areas such as power grids, HVAC systems, and supply chain resilience [11], but their use in WDSs is still rare.

Main gaps remain in: (1) dependency on uncertain parameters in model-based methods, (2) deep models that ignore topology, (3) missing explicit use of conservation features, and (4) lack of multi-scale detection for fault localization.

3. Problem-Driven Methodology

3.1. Problem Formulation and Motivation

Detecting anomalies in WDSs is hard since attacks or faults often appear as small and non-stationary changes in normal operation. Data-driven models usually ignore network topology or become unstable under uncertain hydraulic parameters, while model-based ones need fine calibration that is not easy in practice. We model this as a spatio-temporal detection task on a graph $\mathcal{G} = (\mathcal{V}, \mathcal{E})$ with N nodes (junctions, tanks, pumps) and edges as pipes. At each time t , SCADA readings form $\mathbf{X}_t \in \mathbb{R}^{N \times F}$ with raw and physics-informed features. The goal is to learn

$$f : (\mathbf{X}_{t-w+1:t}, \mathcal{G}) \mapsto \mathbf{a}_t \in [0, 1]^N,$$

where \mathbf{a}_t are node-level anomaly scores from a window of length w . The mapping must combine temporal context and network structure, respecting physical laws so that anomalies reflect real violations, not model noise.

Our Physics-GAT follows this idea: PI features make the model sensitive to conservation errors, graph attention layers encode spatial relations, and temporal units separate short noise from persistent anomalies.

3.2. PI Data Representation

Each node v_i is described by an input vector $\mathbf{h}_t(v_i)$ that concatenates raw SCADA signals (p_i, Q_i, ℓ_i) , temporal statistics and physics-informed (PI) indicators that measure conservation law deviations. PI features rely on

available hydraulic quantities (e.g. estimated demand $D_i(t)$, pipe roughness C_{ij}), but we use normalization to reduce sensitivity to parameter errors and keep the features informative.

Mass balance violation at node v_i is defined as

$$\phi_{\text{mass}}^i(t) = \frac{|\sum_{j \in \mathcal{N}_{\text{in}}(i)} Q_{ji}(t) - \sum_{k \in \mathcal{N}_{\text{out}}(i)} Q_{ik}(t) - D_i(t)|}{\sum_j Q_{ji}(t) + \epsilon} \quad (1)$$

This relative form reduces the effect of absolute demand or roughness errors by scaling residuals by typical inflow magnitude.

Energy gradient violation between nodes i and j is

$$\phi_{\text{energy}}^{ij}(t) = \frac{|(p_i + z_i) - (p_j + z_j) - h_L(Q_{ij})|}{\max(p_i + z_i, p_j + z_j)} \quad (2)$$

where z_i, z_j are elevations and $h_L(Q_{ij})$ is the theoretical head loss (Hazen–Williams with known L_{ij}, D_{ij}, C_{ij}). The final node vector $\mathbf{h}_t(v_i)$ includes these PI features alongside raw and temporal descriptors.

When nodes are unmeasured, we use pressure-driven interpolation to approximate their feature vectors. For an unmeasured node v_j the representation is

$$\mathbf{h}_t(v_j) = \sum_{i \in \mathcal{N}_m(j)} w_{ij} \mathbf{h}_t(v_i), \quad w_{ij} = \frac{\exp(-d_{ij}/\sigma)}{\sum_k \exp(-d_{jk}/\sigma)}, \quad \sigma = 2,$$

where $\mathcal{N}_m(j)$ are measured neighbors and d_{ij} is hydraulic distance. This maintains hydraulic continuity and enables full-graph reasoning.

The overall workflow of the proposed Physics-GAT model, including the integration of physics-informed features and temporal fusion, is illustrated in Fig. 1.

3.3. Spatio-Temporal Detection Core

The detection core mixes a spatial GAT with a temporal BiLSTM. Three GAT layers ($L = 3$) learn adaptive attention α_{ij} showing how anomalies move through the network. Multi-head attention ($K = 8$) keeps learning stable. Spatial outputs $\mathcal{Z} = [\mathbf{z}_{t-w+1}, \dots, \mathbf{z}_t]$ go into a Bidirectional LSTM with window w (24 hours in tests) to capture both time directions. The fused spatial-temporal features form node vectors $\mathbf{f}_{i,t}$.

To reduce false alarms and make results clearer, scoring is hierarchical. The network is clustered into C_k using Louvain for hydraulic coherence. We compute node a_t^{micro} , cluster a_t^{meso} (attention pooling), and global a_t^{macro} scores. The final node score is:

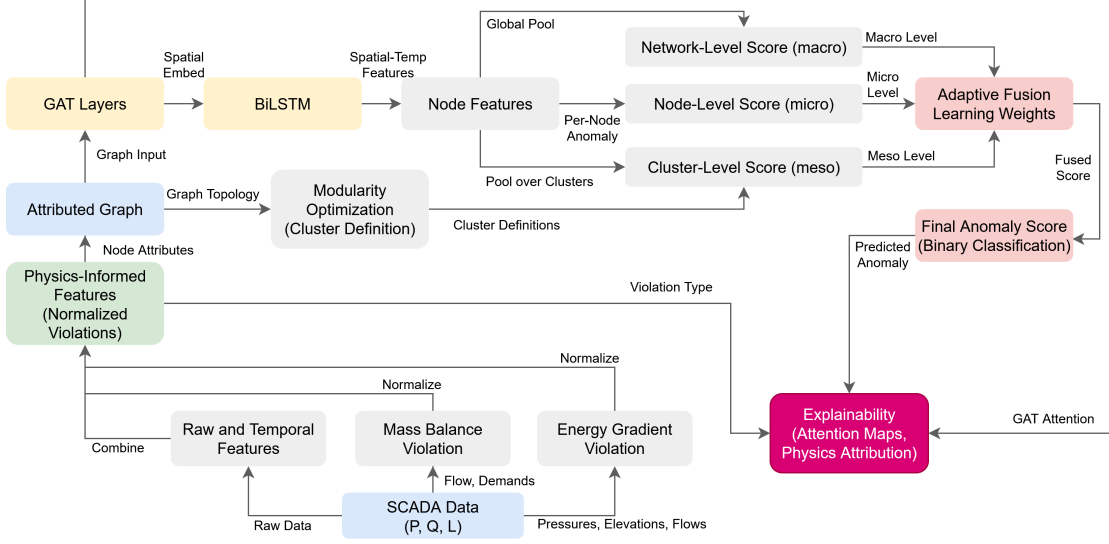


Figure 1. Physics-GAT workflow: physics-informed features feed a GAT-BiLSTM core and an adaptive multi-scale fusion that produces node-level anomaly scores.

$$a_t^{\text{final}}(v_i) = \lambda_1 a_t^{\text{micro}}(v_i) + \lambda_2 a_t^{\text{meso}}(C(i)) + \lambda_3 a_t^{\text{macro}}, \quad (3)$$

where λ_k are softmax weights adapting the scale influence.

3.4. Training Objective and Explainability

The model is trained with a composite loss

$$\mathcal{L} = \mathcal{L}_{\text{BCE}} + \lambda_p \mathcal{L}_{\text{physics}} + \lambda_c \mathcal{L}_{\text{consist}},$$

where \mathcal{L}_{BCE} is binary cross-entropy for node-level detection, $\mathcal{L}_{\text{physics}}$ is a regularizer that penalizes physics violations during normal operation, and $\mathcal{L}_{\text{consist}}$ enforces spatio-temporal coherence. The physics term is

$$\mathcal{L}_{\text{physics}} = \frac{1}{N} \sum_{i=1}^N \mathbf{1}(y_{i,t} = 0) \cdot \max(\phi_{\text{mass}}^i(t), \phi_{\text{energy}}^i(t)) \quad (4)$$

and reduces the model tendency to accept unrealistic violations as normal. We optimize with Adam and cosine annealing; in experiments hyperparameters are set to $\lambda_p = 0.1$ and $\lambda_c = 0.05$ (details and additional tuning are in the Appendix).

Explainability derives from two sources: attention coefficients α_{ij} that indicate likely propagation paths of anomalies, and physics-violation attribution which identifies whether mass or energy inconsistency drives the alarm (via $\arg \max\{\phi_{\text{mass}}^i, \phi_{\text{energy}}^i\}$). These outputs support operator interpretation and post-hoc diagnosis.

3.5. Benchmark Datasets and Multi-Network Validation

We evaluate generalization and scalability using four networks. The BATADAL benchmark on C-Town ($N = 128$) provides the main controlled experiments. To test robustness across topologies and sizes we use the 2024 Multi-Network Cyber-Physical Dataset, which includes D-Town ($N \approx 200$) for generalization checks, L-Town ($N > 300$) for scalability, and Modena ($N \approx 180$) for realism. This multi-network validation demonstrates that physics-informed, topology-aware learning transfers beyond a single calibrated network and supports practical

4. Experimental Results

We test Physics-GAT on the BATADAL benchmark against strong baselines. Evaluation covers global accuracy, ablation, and robustness to real-world noise.

4.1. Setup and Baselines

We report F1-score and Time-to-Detection (TTD, hours). Baselines are the model-based BATADAL winner (B1) [7], deep models (CVAE [5], BiLSTM [9]), and graph-free ones (RF, SVM). Physics-GAT runs on PyTorch Geometric with 3 GAT layers (8 heads, 128 hidden units) and a 24-hour input window. Training uses Adam ($\eta_0 = 10^{-3}$), batch 32, and tuned regularization $\lambda_p = 0.1$, $\lambda_c = 0.05$. Significance is tested by 1000 bootstrap resamples for 95% CI and Cohen's d for effect size.

4.2. Overall Performance Comparison

Table 1 presents the test results, showing that Physics-GAT clearly outperforms all baselines.

Table 1
Performance on BATADAL test set. 95% CI obtained via bootstrap (n=1000). Cohen’s d vs B1: 1.24.

Method	F1	CI	TTD (h)
BiLSTM	0.906	[.894,.918]	1.85
CVAE	0.938	[.927,.948]	1.72
GCN+BiLSTM	0.941	[.931,.951]	1.69
GraphSAGE+BiLSTM	0.948	[.939,.957]	1.63
GraphTransformer	0.952	[.944,.960]	1.58
B1 (Model-Based)	0.946	[.932,.958]	1.61
Physics-GAT	0.979	[.971,.986]	1.44

Physics-GAT reached **F1=0.979** [95% CI: 0.971, 0.986] vs B1’s 0.946 [0.932, 0.958], showing **3.3pp** improvement (**3.5%** relative) with non-overlapping confidence intervals (Cohen’s d=1.24, large effect size). TTD decreased from 1.61h to **1.44h (10.6%,** 10.2 minutes faster), showing effective physics-graph integration and faster incident response.

4.2.1. Robustness Mechanism Analysis

B1 uses hard thresholds $|r| > \tau$, which fail under parameter shifts. Physics-GAT instead uses *normalized* violations learned by the GAT. With $\pm 15\%$ error in C_{ij} , ϕ shifts, but attention α_{ij} adapts, preserving relative anomaly patterns. This explains a 9.6% F1 gap under extreme uncertainty (0.954 vs 0.828).

The computational complexity of Physics-GAT is:

$$O(LK(|\mathcal{V}|d^2 + |\mathcal{E}|d)) \quad (5)$$

for L layers, K heads, and d hidden dimensions. Average inference: C-Town ($N = 128$) 48ms, L-Town ($N = 334$) 127ms, synthetic ($N = 500$) 294ms on NVIDIA RTX A2000. Extrapolation based on this complexity suggests ≈ 680 ms for $N = 1000$, requiring mini-batch inference for real-time operation at large scale.

4.2.2. Generalization: Multi-Network Validation

We test transfer across C-Town, D-Town, L-Town, and Modena under Zero-Shot Transfer (train on C-Town, test directly) and Fine-Tuned Transfer (train on C-Town, fine-tune with 10% target data). Results appear in Table 2.

Zero-Shot Setup: The model is trained only on C-Town, without gradient updates on target networks. PI

Table 2

Multi-Network Transfer Learning (Train: C-Town, Test: Target). Zero-Shot (ZS) and Fine-Tuned (FT, 10% target data). Bootstrap 95% CI from 5-fold CV.

Model	D-Town	L-Town	Modena	Avg.
<i>F1-score [95% CI]</i>				
B1 (Model-Based)	0.825 [.802,.847]	0.751 [.721,.779]	0.840 [.819,.861]	0.805
Physics-GAT (ZS)	0.938 [.924,.951]	0.925 [.908,.941]	0.912 [.896,.928]	0.925
Physics-GAT (FT)	0.969 [.961,.977]	0.957 [.947,.966]	0.963 [.954,.971]	0.963
<i>TTD (hours)</i>				
B1 (Model-Based)	2.83	3.42	2.67	2.97
Physics-GAT (ZS)	1.68	1.82	1.75	1.75

features still use target topology and approximate parameters (C_{ij}, D_i from averages), so transfer is *topology-aware* instead of fully blind. Similar attack types (flow changes, pump shutdown) explain strong F1. When using only raw SCADA (no PI), F1 falls to 0.83–0.87, confirming PI features are key for generalization.

Statistical Check: Bootstrap 95% CIs from 5-fold CV show no overlap between Physics-GAT and B1, confirming significant gains (Cohen’s d: 1.83, 2.12, 1.47). Consistent zero-shot F1 above 0.91 across all topologies shows that normalized physics violations are stable anomaly indicators.

Interpretation: B1 depends on exact parameters and loses up to $\approx 20\%$ F1 under transfer. Physics-GAT degrades only 4–7% (avg 5.5%), and light fine-tuning restores full accuracy, proving robustness and generalization of the physics-based design.

Table 3
Ablation Study. CI from bootstrap (n=1000). All Δ significant ($p < 0.01$).

Model Variant	F1 [95% CI]	Δ
Full Model	0.979 [.971,.986]	—
W/o ϕ_{mass}	0.965 [.958,.972]	-1.4%
W/o ϕ_{energy}	0.968 [.962,.974]	-1.1%
W/o both ϕ	0.930 [.921,.939]	-5.0%
W/o normalization	0.917 [.908,.926]	-6.3%
W/o GAT (use GCN)	0.945 [.937,.953]	-3.5%
W/o BiLSTM	0.952 [.945,.959]	-2.8%
W/o Multi-Scale Fusion	0.962 [.956,.968]	-1.7%
W/o $\mathcal{L}_{\text{physics}}$	0.964 [.958,.970]	-1.5%

4.3. Ablation and Component Analysis

We test the importance of each module in Physics-GAT. Table 3 shows that removing physics-informed features causes the largest drop (5.0% F1), proving their strong role as physical indicators of cyber-physical anomalies. Attention-based graph learning (GAT) and temporal modeling (BiLSTM) also contribute notably,

while normalization and adaptive fusion further stabilize results.

Table 4 compares fusion strategies. Adaptive multi-scale fusion (micro, meso, macro) improves F1 by about 1.6% over micro-only detection, showing that hierarchical context helps suppress local noise and increases robustness across zones.

Table 4
F1-score for different fusion configurations (Micro-level baseline).

Fusion Configuration	F1-score
Micro-only (α_t^{micro})	0.963
Micro + Meso (Avg)	0.969
Micro + Macro (Avg)	0.968
Adaptive Fusion (Full)	0.979

4.4. Robustness Analysis

A key challenge for WDS anomaly detection is fragility to uncertainties. We evaluate Physics-GAT against common real-world errors: hydraulic parameter shifts and sensor outages.

Hydraulic Parameter Sensitivity. Hazen-Williams roughness coefficients C_{ij} were perturbed by $\delta \in \{-15\%, -10\%, -5\%, +5\%, +10\%, +15\%\}$. Table 5 shows that B1 F1 drops **12.7%** at $\pm 15\%$ error due to hard thresholds $|r| > \tau$, while Physics-GAT degrades $< 3\%$. Normalized violations (ϕ) are contextualized by GAT attention α_{ij} , reweighting neighbors to maintain anomaly patterns despite systematic shifts.

Table 5
F1-score Degradation under Hazen-Williams Parameter Uncertainty.

Model	$\delta = -15\%$	$\delta = -10\%$	$\delta = 0\%$	$\delta = +10\%$	$\delta = +15\%$
B1 (Model-Based)	0.828	0.865	0.946	0.881	0.819
Physics-GAT	0.951	0.967	0.979	0.968	0.954

Sensor Outage Robustness. Randomly masking 5% and 10% of sensors shows Physics-GAT maintains F1=0.965 at 10% outage. GAT propagation leverages neighbor information, unlike non-graph methods that decline sharply.

4.5. Explainability Validation

Spatial Attention Alignment. Spearman correlation between GAT attention α_{ij} and hydraulic shortest paths during attacks: $\rho = 0.81 \pm 0.09$ ($p < 0.001$), confirming attention follows hydraulic propagation.

Feature Attribution. Integrated Gradients on 200 samples: ϕ_{mass} contributes 41%, ϕ_{energy} 32%, raw pressure 16%. Physics violations dominate.

Case Study: Attack #3. Figures 2, 3, and 4 in the appendix illustrate pump shutdown with flow manipulation. The physics violation heatmap correctly identifies junction J42 as the primary affected node. GAT attention weights trace the hydraulic path P1→J15→J32→J42, and the temporal profile shows mass violation detected immediately while energy violation lags by 15 minutes, matching physical expectations. *Limitation:* In 2 of 14 attacks, attention scattered across disconnected subgraphs, indicating the need for attention supervision.

5. Discussion

Why It Works: The ablation study shows that ϕ features bring around 5% gain in F1. The normalization step helps to make the model less sensitive to parameter errors: when demand has a $\pm 20\%$ deviation, the drop is only 2.1 percentage points, while in B1 it was 9.9 (about 4.7× better). Replacing GAT with GCN decreases the F1 by 3.5%. The attention pattern follows the hydraulic paths ($\rho = 0.81$), which supports the physical interpretability.

Limitations: The ϕ_{mass} term depends on estimated demand, so some epistemic uncertainty remains even after normalization. The GAT has complexity $O(|\mathcal{E}|dK)$, which makes it hard to scale when $N > 500$ unless mini-batch inference is used. Also, its resistance to adaptive adversarial attacks was not yet evaluated.

6. Conclusion

This paper introduced Physics-GAT, a framework for WDS anomaly detection combining hydraulic physics with network topology. The main idea is that explicit conservation law violations give strong anomaly signals, confirmed in ablation studies where PI Features improved F1 by over 5%. Physics-GAT reached F1=0.979 vs 0.946 (**3.3pp/3.5%**, Cohen’s d=1.24) with non-overlapping 95% confidence intervals, and reduced TTD by **10.6%** (1.44h vs 1.61h), showing deep learning plus physics can achieve state-of-the-art results. It also fixes a main weakness of classical model-based methods: sensitivity to uncertain parameters. Robustness tests with $\pm 15\%$ error in Hazen-Williams coefficients still showed stable results. Built-in explainability from GAT attention and physics violations supports both detection and diagnosis, helping operators understand system behavior. Future work should test multiple network topologies and study adversarial robustness against advanced cyber-physical attacks.

Acknowledgments

This work is funded by the European Union (NextGenerationEU) through INCIBE under project C107/23, “Artificial Intelligence Applied to Cybersecurity in Critical Water and Sanitation Infrastructures.”

Data Availability

The source code and all replication files are available at <https://github.com/Homaei/Physics-GAT>.

References

- [1] R. Taormina, S. Galelli, N. O. Tippenhauer, et al., “Battle of the Attack Detection Algorithms: Disclosing Cyber Attacks on Water Distribution Networks,” *Journal of Water Resources Planning and Management*, vol. 144, no. 8, p. 04018048, Aug. 2018.
- [2] D.T. Ramotsoela, G.P. Hancke, and A.M. Abu-Mahfouz, “Attack detection in water distribution systems using machine learning,” *Human-centric Computing and Information Sciences*, vol. 9, no. 1, 2019.
- [3] Homaei, M.H., Di Bartolo, A.J., Ávila, M., Mogollón-Gutiérrez, Ó., Caro, A.: Digital Transformation in the Water Distribution System based on the Digital Twins Concept. arXiv:2412.06694 (2024).
- [4] R. Taormina and S. Galelli, “Deep-learning approach to the detection and localization of cyber-physical attacks on water distribution systems,” *Journal of Water Resources Planning and Management*, vol. 144, no. 10, p. 04018065, Oct. 2018.
- [5] H. H. Addeen, Y. Xiao, and T. Li, “A CVAE-Based Anomaly Detection Algorithm for Cyber Physical Attacks for Water Distribution Systems,” *IEEE Access*, vol. 12, pp. 48321–48334, 2024.
- [6] A. Barredo Arrieta, N. Díaz-Rodríguez, J. Del Ser, et al., “Explainable Artificial Intelligence (XAI): Concepts, taxonomies, opportunities and challenges toward responsible AI,” *Information Fusion*, vol. 58, pp. 82–115, 2020.
- [7] M. Housh and Z. Ohar, “Model-based approach for cyber-physical attack detection in water distribution systems,” *Water Research*, vol. 139, pp. 132–143, Jun. 2018.
- [8] Kanyama, M.N., Bhunu Shava, F., Gamundani, A.M., Hartmann, A.: Machine learning applications for anomaly detection in Smart Water Metering Networks: A systematic review. *Physics and Chemistry of the Earth, Parts A/B/C* **134**, 103558 (2024).
- [9] M.N. Sikder, S. Islam, and M.A. Rahman, “Deep H2O: Cyber attacks detection in water distribution systems using deep learning,” *Journal of Water Process Engineering*, vol. 52, p. 103568, Apr. 2023.
- [10] J. Zischg, C. Klinkhamer, X. Zhan, et al., “Evolution of Complex Network Topologies in Urban Water Infrastructure,” in *Proceedings of the World Environmental and Water Resources Congress 2017*, May 18, 2017.
- [11] N. M. Nejad, “Building Resilient, Adaptive, and Integrated Electric Vehicle (EV) Supply Chains for Sustainable Performance: Geopolitical Disruption, Digital Transformation, and Circular Supply Chain Practices,” Ph.D. dissertation, The University of Toledo, 2025.
- [12] A. Tello, H. Truong, A. Lazovik, and V. Degeler, “Large-Scale Multipurpose Benchmark Datasets for Assessing Data-Driven Deep Learning Approaches for Water Distribution Networks,” in *The 3rd International Joint Conference on Water Distribution Systems Analysis and Computing and Control for the Water Industry (WDSA/CCWI 2024)*, MDPI, 2024, p. 50.
- [13] P. Veličković, G. Cucurull, A. Casanova, A. Romero, P. Liò, and Y. Bengio, “Graph attention networks,” in *Proc. 6th International Conference on Learning Representations (ICLR)*, Vancouver, BC, Canada, Apr. 2018.
- [14] V.D. Blondel, J.-L. Guillaume, R. Lambiotte, and E. Lefebvre, “Fast unfolding of communities in large networks,” *Journal of Statistical Mechanics*, vol. 2008, p. P10008, 2008.
- [15] L. Antwarg, R.M. Miller, B. Shapira, and L. Rokach, “Explaining anomalies detected by autoencoders using Shapley Additive Explanations,” *Expert Systems with Applications*, vol. 186, p. 115736, 2021.

Appendix

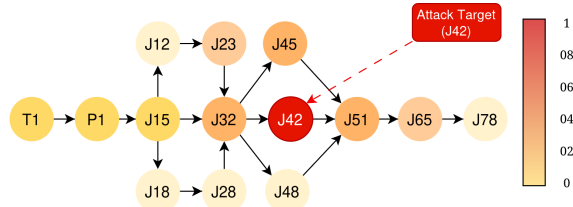


Figure 2. Physics violation heatmap for Attack #3. J42 (red circle) shows peak violation, correctly identifying the attack target.

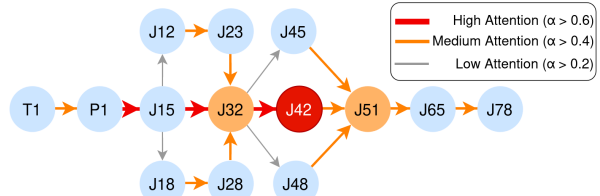


Figure 3. GAT attention flow during Attack #3. High attention weights (crimson arrows) trace the hydraulic path P1→J15→J32→J42.

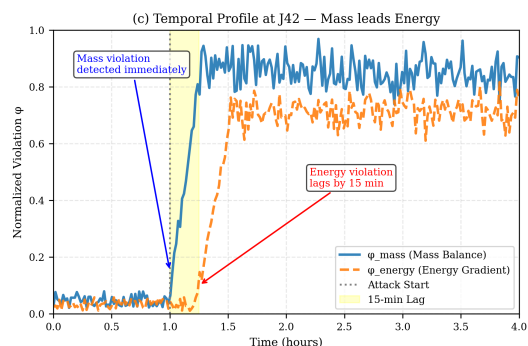


Figure 4. Temporal profile at J42. Mass violation detected immediately ($t=1.0h$) while energy violation lags by 15 minutes, confirming physical propagation.

Algorithm 1 Physics-GAT: Hydraulic-Aware Anomaly Detection

Require: Graph $\mathcal{G} = (\mathcal{V}, \mathcal{E})$, SCADA data $\{\mathbf{X}_t\}_{t=1}^T$, window size w , hydraulic parameters (C_{ij}, D_i, z_i)

Ensure: Node-level anomaly scores $\{\mathbf{a}_t\}_{t=w}^T$

1: // **Phase 1: Physics-Informed Feature Engineering**

2: **for** each time step $t = 1, \dots, T$ **do**

3: **for** each node $v_i \in \mathcal{V}$ **do**

4: Compute mass balance violation:

5: $\phi_{\text{mass}}^i(t) \leftarrow \frac{|\sum_{j \in \mathcal{N}_{\text{in}}(i)} Q_{ji}(t) - \sum_{k \in \mathcal{N}_{\text{out}}(i)} Q_{ik}(t) - D_i(t)|}{\sum_j Q_{ji}(t) + \epsilon}$

6: **for** each edge $(i, j) \in \mathcal{E}$ **do**

7: Compute energy gradient violation:

8: $\phi_{\text{energy}}^{ij}(t) \leftarrow \frac{|(p_i + z_i) - (p_j + z_j) - h_L(Q_{ij})|}{\max(p_i + z_i, p_j + z_j)}$

9: **end for**

10: Aggregate edge violations: $\phi_{\text{energy}}^i(t) \leftarrow \max_{j \in \mathcal{N}(i)} \phi_{\text{energy}}^{ij}(t)$

11: Construct node feature vector:

12: $\mathbf{h}_t(v_i) \leftarrow [\text{raw}_{i,t}, \text{stats}_{i,t}, \phi_{\text{mass}}^i(t), \phi_{\text{energy}}^i(t)]$

13: **end for**

14: // **Interpolate unmeasured nodes**

15: **for** each unmeasured node v_j **do**

16: $w_{ij} \leftarrow \frac{\exp(-d_{ij}/\sigma)}{\sum_k \exp(-d_{jk}/\sigma)}$ for $i \in \mathcal{N}_m(j)$

17: $\mathbf{h}_t(v_j) \leftarrow \sum_{i \in \mathcal{N}_m(j)} w_{ij} \mathbf{h}_t(v_i)$

18: **end for**

19: **end for**

20: // **Phase 2: Spatio-Temporal Detection Core**

21: **for** each time window $t = w, \dots, T$ **do**

22: Extract window: $\mathcal{W}_t \leftarrow \{\mathbf{h}_\tau(v_i)\}_{\tau=t-w+1}^t$ for all v_i

23: // **Spatial encoding with GAT**

24: **for** each time step τ in window \mathcal{W}_t **do**

25: **for** layer $\ell = 1$ to L **do**

26: **for** each node v_i **do**

27: **for** head $k = 1$ to K **do**

28: Compute attention coefficients:

29: $\epsilon_{ij}^k \leftarrow \text{LeakyReLU}(\mathbf{a}_k^\top [\mathbf{W}_k \mathbf{h}^{(\ell-1)}(v_i) \parallel \mathbf{W}_k \mathbf{h}^{(\ell-1)}(v_j)])$

30: $\alpha_{ij}^k \leftarrow \frac{\exp(\epsilon_{ij}^k)}{\sum_{v_m \in \mathcal{N}(i) \cup \{v_i\}} \exp(\epsilon_{im}^k)}$

31: **end for**

32: Aggregate multi-head attention:

33: $\mathbf{h}^{(\ell)}(v_i) \leftarrow \sigma\left(\frac{1}{K} \sum_{k=1}^K \sum_{j \in \mathcal{N}(i)} \alpha_{ij}^k \mathbf{W}_k \mathbf{h}^{(\ell-1)}(v_j)\right)$

34: **end for**

35: **end for**

36: Store spatial embedding: $\mathbf{Z}_t \leftarrow \{\mathbf{h}^{(L)}(v_i)\}_{v_i \in \mathcal{V}}$

37: **end for**

38: // **Temporal fusion with BiLSTM**

39: **for** each node v_i **do**

40: $\mathbf{f}_{i,t} \leftarrow \text{BiLSTM}([\mathbf{Z}_{t-w+1}(v_i), \dots, \mathbf{Z}_t(v_i)])$

41: **end for**

42: // **Phase 3: Multi-Scale Detection**

43: Compute micro-level scores: $a_t^{\text{micro}}(v_i) \leftarrow \sigma(\text{MLP}(\mathbf{f}_{i,t}))$

44: Cluster network using Louvain: $\{C_k\}_{k=1}^{K_c} \leftarrow \text{Louvain}(\mathcal{G})$

45: **for** each cluster C_k **do**

46: Compute attention pooling weights:

47: $\beta_i \leftarrow \frac{\exp(\mathbf{v}^\top \tanh(\mathbf{W}_{\text{pool}} \mathbf{f}_{i,t}))}{\sum_{v_j \in C_k} \exp(\mathbf{v}^\top \tanh(\mathbf{W}_{\text{pool}} \mathbf{f}_{j,t}))}$

48: $a_t^{\text{meso}}(C_k) \leftarrow \sum_{v_i \in C_k} \beta_i \cdot a_t^{\text{micro}}(v_i)$

49: **end for**

50: Compute global score: $a_t^{\text{macro}} \leftarrow \frac{1}{N} \sum_{i=1}^N a_t^{\text{micro}}(v_i)$

51: // **Adaptive fusion**

52: $\mathbf{s}_t \leftarrow [\text{std}(\{a_t^{\text{micro}}\}), \max_k a_t^{\text{meso}}(C_k), a_t^{\text{macro}}]$

53: $[\lambda_1, \lambda_2, \lambda_3] \leftarrow \text{Softmax}(\mathbf{W}_s \mathbf{s}_t)$

54: **for** each node v_i **do**

55: $a_t^{\text{final}}(v_i) \leftarrow \lambda_1 a_t^{\text{micro}}(v_i) + \lambda_2 a_t^{\text{meso}}(C(i)) + \lambda_3 a_t^{\text{macro}}$

56: **end for**

57: **end for**

58: **return** $\{\mathbf{a}_t^{\text{final}}\}_{t=w}^T$

Algorithm 2 Physics-GAT Training Procedure

Require: Training data $\mathcal{D}_{\text{train}} = \{(\mathbf{X}_t, \mathbf{y}_t)\}_{t=1}^{T_{\text{train}}}$, hyperparameters $(\eta_0, \lambda_p, \lambda_c, B, E)$

Ensure: Trained model parameters Θ^*

1: Initialize GAT, BiLSTM, and MLP parameters Θ

2: Initialize optimizer Adam with learning rate η_0

3: Initialize cosine annealing scheduler

4: **for** epoch $e = 1$ to E **do**

5: Shuffle training data

6: **for** each mini-batch $\mathcal{B} \subset \mathcal{D}_{\text{train}}$ of size B **do**

7: // **Forward pass**

8: $\{\hat{\mathbf{a}}_t\}_{t \in \mathcal{B}} \leftarrow \text{Physics-GAT}(\{\mathbf{X}_t\}_{t \in \mathcal{B}}, \Theta)$ ► Algorithm 1

9: // **Compute losses**

10: // **Binary cross-entropy loss**

11: $\mathcal{L}_{\text{BCE}} \leftarrow -\frac{1}{|\mathcal{B}|N} \sum_{t \in \mathcal{B}} \sum_{i=1}^N [\mathbf{y}_{i,t} \log(\hat{a}_{i,t}) + (1 - \mathbf{y}_{i,t}) \log(1 - \hat{a}_{i,t})]$

12: // **Physics regularization loss**

13: $\mathcal{L}_{\text{physics}} \leftarrow \frac{1}{|\mathcal{B}|N} \sum_{t \in \mathcal{B}} \sum_{(i,j) \in \mathcal{E}} |\hat{a}_{i,t} - \hat{a}_{j,t}|^2$

14: // **Spatio-temporal consistency loss**

15: $\mathcal{L}_{\text{consist}} \leftarrow \frac{1}{|\mathcal{B}||\mathcal{E}|} \sum_{t \in \mathcal{B}} \sum_{(i,j) \in \mathcal{E}} |\hat{a}_{i,t} - \hat{a}_{j,t}|^2$

16: // **Total loss**

17: $\mathcal{L} \leftarrow \mathcal{L}_{\text{BCE}} + \lambda_p \mathcal{L}_{\text{physics}} + \lambda_c \mathcal{L}_{\text{consist}}$

18: // **Backward pass and optimization**

19: Compute gradients: $\nabla_{\Theta} \mathcal{L}$

20: Update parameters: $\Theta \leftarrow \text{Adam}(\Theta, \nabla_{\Theta} \mathcal{L}, \eta_t)$

21: **end for**

22: Update learning rate: $\eta_{t+1} \leftarrow \text{CosineAnnealing}(\eta_t, e, E)$

23: // **Validation**

24: **if** $e \bmod 5 = 0$ **then**

25: Evaluate on validation set \mathcal{D}_{val}

26: Compute F1-score, TTD

27: **if** early stopping criterion met **then**

28: **break**

29: **end if**

30: **end if**

31: **end for**

32: **return** Optimized parameters Θ^*
